Results in Chemistry 13 (2025) 102050

Contents lists available at ScienceDirect

Results in Chemistry

journal homepage: www.sciencedirect.com/journal/results-in-chemistry

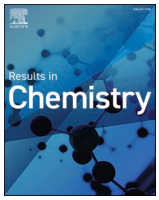

Ball-milled synthesis of biochar-MOF nanocomposite for the concurrent recovery of mixed contaminants from wastewater

Sefiu Olaitan Amusat [a], Temesgen Girma Kebede [a,*], Edward Ndumiso Nxumalo [b], Simiso Dube [a], Mathew Muzi Nindi [b]

[a] Department of Chemistry, College of Science, Engineering, and Technology, University of South Africa, The Science Campus, Florida Park, Corner Christian de Wet & Pioneer Avenue, Florida 1709 Johannesburg, South Africa
[b] Institute for Nanotechnology and Water Sustainability (iNanoWS), College of Science, Engineering, and Technology, The Science Campus, University of South Africa, Corner Christian de Wet & Pioneer Avenue Florida Park, 1709 Johannesburg, South Africa

ARTICLE INFO

Keywords:
Metal–organic framework (MOF)
Biochar
Enhanced functionalities
Wastewater remediation
Green solvent-free
Textural morphology
Ball milling

ABSTRACT

In this study, a biochar-metal–organic framework (MOF) nanocomposite was synthesized via ball milling to enable the simultaneous extraction of multiple contaminants from wastewater. The Brunauer-Emmett-Teller (BET) analysis revealed a significant increase in surface area after ball milling. SEM-EDS confirmed the successful synthesis, while X-ray diffraction (XRD) and thermogravimetric analysis (TGA) indicated an amorphous structure with thermal stability up to 300 °C. FTIR and XPS analyses identified functional groups such as C=C, C-H, –COOH, C=O, –OH, C-O, and Fe-BTC. Adsorption capacity and binding properties were evaluated using Langmuir and Freundlich isotherms, with the Freundlich model providing a better fit (R^2 = 0.9579–0.9913) compared to the Langmuir model (R^2 = 0.9239–0.9862). The nanocomposite exhibited maximum adsorption capacities of 74.18–85.69 mgg^{-1} for heavy metals and 72.99–86.21 mgg^{-1} for steroidal hormones. Kinetic analysis showed the adsorption process followed a pseudo-second-order model. A leaching test confirmed the nanocomposite's high stability, making the BC-Fe-BTC nanocomposite a promising material for wastewater treatment applications.

1. Introduction

Water is essential for all life on Earth, but clean and accessible water sources are being depleted due to rising demand driven by rapid urbanization and population growth [1]. An increase in agricultural production is required to meet the growing demand for food, thus competition for scarce water resources is expected to increase. Even though water is indispensable and the most important resource in the world, it is now being most adversely impacted by contamination because of the growing population [2]. A significant amount of harmful heavy metals is released into water, the soil, or the surface due to human activities which include mining and smelting, pesticides, fertilizers, and herbicides application and other activities [3]. Due to their toxicity, even in trace amounts, heavy metal pollution has been a subject of concern throughout the world [4]. Accumulation of these heavy metals such as lead, cadmium and arsenic can affect the endocrine system in the human body as well as other biological functions [5,6]. Removal of heavy metals (HMs) from contaminated water and wastewater is a crucial step to enable the reuse of these water resources.

Additionally, emerging contaminants (ECs) have gained attention recently due to their detrimental consequences on people and the ecosystem of living organisms [7]. Because these pollutants are resistant to conventional water and wastewater treatment methods, their presence in water is of concern [8]. A few examples of emerging pollutants are pharmaceuticals, substances like hormone-disrupting chemicals, fire retardants, cleaning agents, insecticides, weed killers, synthetic sweeteners, and personal hygiene items [9]. The result of continuous accumulation of these steroidal hormones may form complexes which are carried to the nucleus, where they impair the systems' neurological, immunological, and reproductive processes [10]. Among the possible dangers they pose to living things include the induction of cancer, interference with regular reproduction, and disruption of apoptotic processes [11–13].

Therefore, there should be an approach to remove these pollutants to mitigate the problems described above due to the presence of toxic organic pollutants and heavy metals in the wastewater. Traditional

* Corresponding author.
E-mail address: kebedtg@unisa.ac.za (T.G. Kebede).

https://doi.org/10.1016/j.rechem.2025.102050
Received 17 August 2024; Accepted 13 January 2025
Available online 15 January 2025

wastewater treatment facilities cannot eliminate contaminants at a trace level; however, numerous treatment techniques have been adopted to remove heavy metals and organic contaminants from wastewater. These techniques include ion exchange, membrane techniques, electrocoagulation, adsorption, precipitation, and chemical oxidation [414151617]. The mentioned technologies, however, present difficulties in the form of sludge creation, drawn-out and tedious operations, and capital-intensive [1819]. Among the technologies discussed above, adsorption is regarded as a practical technique for contaminants from wastewater [20]. Adsorption is an effective and economical method for purifying wastewater, widely valued for its simplicity and ability to remove harmful organic and inorganic substances [21].

Moreover, inexpensive adsorbent materials are currently receiving much consideration for the adsorption of pollutants. Numerous adsorbent materials have also been applied in removing pollutants from the wastewater, and these adsorbents include clays, charcoal fly ash, brick dust, quartz and granite, husk, seed, bark, water-soluble protein, activated carbon, activated alumina, silica, polymers, nanomaterials, and biochar. [2223242526]. Biochar stands out as a cost-effective adsorbent, distinguished for its efficacy in eliminating contaminants. [27]. It has also been used as fuel, adsorbents, catalytic supports, and even as a catalyst. [28]. Biochar has demonstrated its effectiveness in removing heavy metals [3], and emerging contaminants from water [29]. Biochar can be made from various inexpensive sources, such as biomass and leftover materials from forestry activities [30]. Adsorbents with high adsorption capacities are necessary frameworks in practical applications. Unfortunately, due to inherent limitations such as a small surface area and low porosity, the pristine biochar exhibits poor adsorption performance. [31]. Lately, there have been suggestions for modification techniques aimed at improving the adsorption capabilities of pure biochar. These include methods involving metal ions, acids, alkaline solutions, and oxidizing agents. [32333435]. Physical modification such as ball milling was used to alter the physical characteristics of biochar, including its pore structure and surface morphology. By impregnating the biochar with acid, alkali, strong oxide, or other chemicals, the biochar undergoes a chemical reaction that changes the properties of the surface. A review article highlighted that nickel and cobalt nanoparticles exhibit magnetic characteristics and are used in a variety of environmental applications, in addition to iron nanoparticles. [36].

Currently, attention is directed towards the modification of biochar with MOF materials for potential usage in water treatment; in particular, stable MOFs are used with a simple preparation method [37]. Porous coordination polymers (PCPs) also known as MOFs, constitute a unique class of porous materials that have garnered substantial attention across various industries. This material has exceptional performance in multiple applications attributed to the distinctiveness of its high dispersion of metal components, crystalline porous structure, and flexible pore size. MOFs have found usage in many scientific disciplines, such as in photocatalysis [38], energy storage [39 40], adsorption, [41] and electrochemical sensing [42].

Metal-organic frameworks (MOFs), a type of porous material, have drawn considerable interest from researchers as promising adsorbents [43]. Their use in dye removal presents a cost-efficient and practical alternative. MOFs, a relatively new class of materials explored over the last 20 years, are defined by their unique porosity [44]. They offer remarkable properties such as high thermal stability, large surface areas essential for adsorption, large pore sizes, and flexible metal sites [45,46].

Owing to their ability to selectively remove contaminants, low cost of production and reusability, MOF composites emerge as sustainable and effective adsorption materials for wastewater treatment. They are effective in removing organic pollutants and volatile organic compounds that result from anthropology. Although they have excellent results in their removal ability of pollutants on the laboratory scale, their commercial application is still in the early stage. These materials are a promising method to eliminate pollutants and promote sustainable water treatment. [47].

A comprehensive review of recent advancements in using MOFs for adsorptive removal of organic pollutants from wastewater was compiled by [48], It has been highlighted that Metal-organic frameworks (MOFs) are important in this application as a novel class of porous adsorbents, known for their highly crystalline molecular structure and large surface area, both of which are crucial factors in adsorption processes. Their adjustable properties also make them a recommended choice for sorbents used in wastewater purification technologies.

In a study investigating the adsorption capabilities of MOFs, MOF-525 was combined with magnetic Fe_3O_4. It was observed that this composite achieved a tetracycline adsorption capacity of 277 mgg^{-1}. Additionally, the separation process and recovery from the solution is very simple, and therefore this material shows great potential for adsorption application [49]. In a recent study by Kase et al, a single-pot hydrothermal method was effectively used to produce a MOF composite sponge adsorbent (Fe_3O_4@Pd-MOF@CSC). The effectiveness of the adsorbent in eliminating indigo carmine blue (ICB) from aqueous solutions was carefully assessed. The results showed that the Langmuir isotherm model could adequately represent the adsorption process of the Fe_3O_4@Pd-MOF@CS composite sponge [50]. In addition, in another recent study one-step method was used to successfully develop a novel citrate-crosslinkedLa-MOF/citrate-crosslinked chitosan composite sponge (La-MOF@CSC composite sponge) in an acidic environment. The research studied the composite sponge affected Hg (II) adsorption and removal of mercury (Hg(II)) from water. The composite sponge had a remarkably high surface area of 1208 m^2g^{-1} and a maximum adsorption capacity (qmax) for Hg (II) of 765.22 mgg^{-1}. The research used the Langmuir isotherm model and pseudo-second-order equations to predict the adsorption isotherm and kinetics of the adsorption respectively [51]. developed an innovative Aluminium-based sensitive sensor material, HPDTP-Al MOF sensor. The sensor was meticulously crafted through the diazotization of the NH_2-MIL53(Al) MOF and coupling it with resorcinol to develop the HPDTP-Al MOF sensor material. The performance, selectivity, and sensitivity of the developed HPDTP-Al MOF were thoroughly evaluated. It successfully detected ultra-trace concentrations of Co^{2+} and Pd^{2+} ions using spectrophotometric and fluorometric methods. The MOF was tested by detecting and removing Co^{2+} in real electroplating wastewater samples. It was also used to recover Pd^{2+} ions from electronic wastes [52].

There are, however, limited research works on the removal of pollutants using biochar-based MOF- nanocomposite derived from porous carbon materials [53].

Ball milling is increasingly accepted as an advantageous, solvent-free, economical, and environmentally benign method for material modification [54]. This approach has been effective in modifying biochar properties, such as enhancing oxygen-containing functional groups, increasing surface area, reducing particle size, and enhancing both adsorption and catalytic properties [2855]. The benefits of ball milling include fast reaction rates, the ability to handle large preparation volumes, minimal or no solvent requirement, and the promotion of metal–organic framework (MOF) synthesis [56]. For example, the creation of CuO/biochar nanocomposites through ball milling has shown substantial dye removal from water [57], and the production of ZnO/biochar nanocomposites has attained a 95% removal efficiency for methylene blue [58]. In the current investigation, ball milling was employed to produce biochar-based/Fe-MOFs, which were then employed for the concurrent extraction of steroid hormones and heavy metals from wastewater. The main aim of this research is to explore the enhancement of biochar by integrating MOF nanocomposites via ball milling process, aiming to simultaneously remove heavy metals and steroid hormones from wastewater.

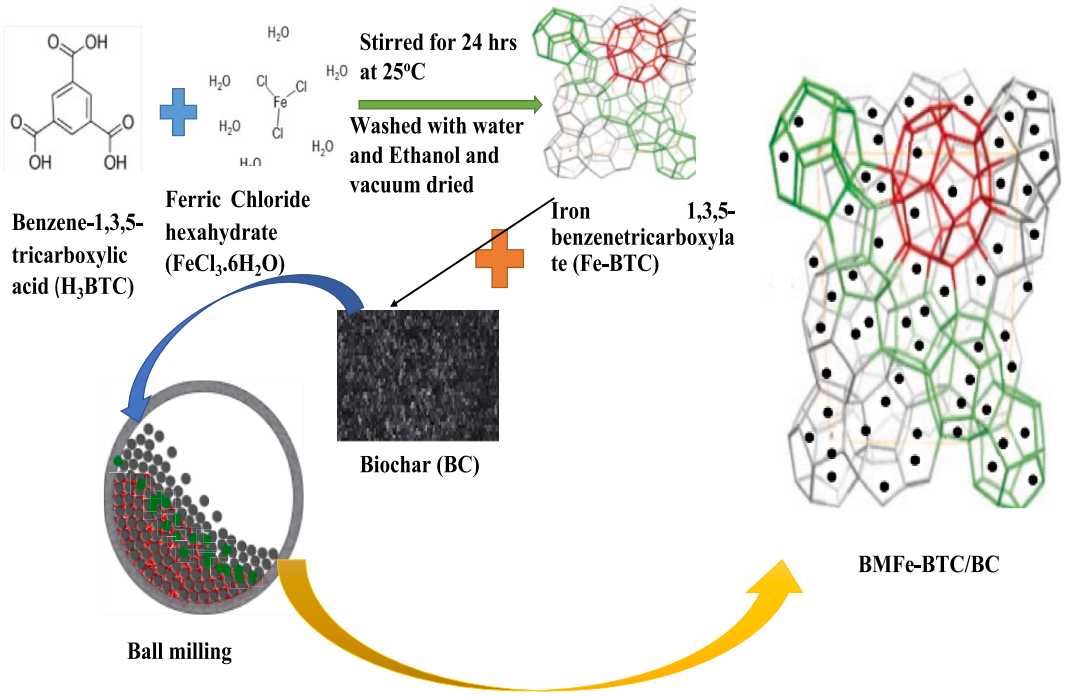

Fig. 1. Schematic sequential steps involved in the preparation of MOF-biochar nanocomposites.

2. Materials and methods

2.1. Materials

The biochar utilized in this investigation was produced through the pyrolysis process of African Star Apple seed pods. Additionally, chemicals comprising ferric chloride ($FeCl_3{\cdot}6H_2O$), benzene-1,3,5-tricarboxylic acid ($H_3BTC(C_9H_6O_6)$), nickel nitrate Ni $(NO_3)_2{\cdot}6H_2O$, cadmium nitrate Cd $(NO_3)_2{\cdot}4H_2O$, sodium hydroxide (NaOH) and lead nitrate Pb $(NO_3)_2$, which are necessary for the experiment were procured from Sigma-Aldrich. The steroid hormones: testosterone, progesterone, β-estradiol, estriol, α-estradiol, and Bisphenol A were included, each with 98% purities. To prepare the stock solutions, each standard (10 mg) was dissolved in a 10-mL volumetric flask containing 1 mL of a 50:50 mixture of methanol and ultrapure water (18.2 Ω/cm), and then the solution was brought to the calibration mark. The dilution of these stock solutions was performed using a dilution formula to attain the required concentrations.

2.2. Preparation of pristine biochar

The biochar utilized in this investigation was prepared using the procedures outlined [59]. A dried feedstock weighing 20 g underwent heating for an hour at 500°C with a heating rate of 10°Cmin^{-1} in a muffle furnace, under controlled oxygen conditions. Subsequently, each batch of prepared biochar was stored in an airtight container labelled ASA550 before being subjected to characterization techniques and subsequent MOF incorporation.

2.3. Preparation of MOF-biochar nanocomposites

As illustrated in Fig. 1, the prepared biochar (1.8 g) and a blend of Fe-BTC MOFs were ball-milled at a rate of 800 rpm for 12 h to create the biochar-Fe-BTC composites. Iron-based MOFs with different mixing ratios of 15%, 25%, and 50% of FeBTC-BC were generated. [60].

2.4. Characterisation of biochar/MOF nanocomposites

The physicochemical attributes of biochar/MOF nanocomposites, encompassing pore size, surface area, and grain structure, were evaluated through Brunauer-Emmett-Teller (BET) analysis, which was performed using a Micromeritics® ASAP™ 2020 instrument, coupled with TriStar™ II version 2.00 software, both supplied by Micromeritics Instrument Corporation. The crystalline structure of the nanocomposites was examined via X-ray diffraction (XRD) analysis, utilizing a Rigaku SmartLab X-Ray diffractometer, at a diffraction angle of 2θ degrees. Fourier-transform infrared (FTIR) spectroscopy, employing a Vertex 70v FT-IR Spectrometer from Bruker Optics, was utilized to detect the surface functional groups within the wavenumber spectrum of 4,000 to 400 cm^{-1}. Scanning electron microscopy (SEM), coupled with an Oxford Instruments energy-dispersive X-ray spectroscopy (EDS) system, specifically a JEOL JSM-IT 300 SEM was utilized to elucidate the elemental composition, structural characteristics, and surface morphology of the nanocomposites. The thermal stability and weight loss profiles of the biochar/MOF nanocomposites were investigated using a thermogravimetric analyser (TGA/DSC SDT Q600 model), complemented by thermal analysis (TA) software. Furthermore, X-ray photoelectron spectroscopy (XPS), employing a Thermo Fisher Scientific™ ESCALAB 250Xi X-ray Photoelectron Spectrometer, was employed to probe the oxidation states and elemental composition of the material surfaces.

2.5. Adsorption experiment of real wastewater

In the adsorption experiment, the adsorbents were investigated with a 50 mg sample immersed in a 25 mL solution that contained a combination of all three heavy metals and steroid hormones at a concentration of 2 mg/L. We experimented at 25°C, with a pH of 6.5, over a contact time of 60 min, and under agitation at 180 rpm. Subsequently, the solutions were passed through a PVDF syringe filter with a pore size of 0.45 μm and a diameter of 25 mm. The resulting filtrates were then gathered in HPLC sample vials and plastic sample tubes for further analysis using ICP-OES. To ascertain the percentage removal of each heavy metal and steroid hormone, Equation (1) was employed. For calculating the amount of each heavy metal and steroid hormone

Table 1
Surface properties of biochar/MOF nanocomposites.

Adsorbent	Surface area S_{BET} (m^2/g)	*BJH pore size (nm)	Grain size (nm)
ASA550	172	3.57	34.70
BASA550	302	6.22	19.84
BMFe-BTC	146	7.61	40.94
15 % FeBTC-BC	159	2.54	22.08
25 % FeBTC-BC	185	4.01	36.20
50 % FeBTC-BC	284	5.32	20.43

*BJH – Barrett-Joyner-Halenda approach.

adsorbed at equilibrium (q_e) by the adsorbent, expressed in milligrams per gram (mg/g), Equation (2) was utilized.

$$\text{Removal}\,\% = \left(\frac{Co - C_e}{C_o}\right) \times 100 \tag{1}$$

The term Co represents the initial concentrations, while Ce is ascribed to the concentrations at the equilibrium, measured in milligrams per litre (mg/L).

$$q_e = \left(\frac{Co - C_e}{m}\right) \times V \tag{2}$$

where:

C_o denotes the initial concentration of heavy metals and steroid hormones in the solution, quantified in milligrams per gram (mgg^{-1}).

C_e signifies the concentration of heavy metals and steroid hormones at equilibrium, similarly, measured in milligrams per gram (mgg^{-1}).

V Indicates the volume of the solution, quantified in litres (L)

m represents the mass of the adsorbent, measured in grams (g).

The linear form of the Freundlich equation can be articulated as follows:

$$\log(q_e) = \log K_f + \frac{1}{n}\log(C_e) \tag{3}$$

where:

C_e (mol/L) indicates the concentration of steroid hormones at equilibrium.

q_e (mg/g) signifies the amount of steroid hormone adsorbed per gram at the equilibrium concentration.

K_F represents the adsorption capacity of the adsorbent.

1/n signifies the adsorption intensity of the adsorbent.

The linear form of the Langmuir equation may be expressed as follows (Equation (4)):

$$\frac{C_e}{q_e} = \frac{1}{q_{max}K_L} + \frac{C_e}{q_{max}} \tag{4}$$

where:

q_{max} (mg/g) represents the adsorbent capacity.

K_L(L/mg) is the Langmuir constant.

q_e signifies the quantity of adsorbate adsorbed at equilibrium, expressed in mg/g.

Ce indicates concentration at equilibrium, expressed in moles per litre (mol/L).

The separation factor (R_L), which is a dimensionless constant, characterizes the Langmuir isotherm and is given by Equation (5).

$$R_L = \frac{1}{1 + K_L C_O} \tag{5}$$

In this study, the Langmuir constant (K_L), and the separation factor (R_L) were investigated. Additionally, the data obtained experimentally were analysed using the pseudo-first and pseudo-second-order kinetic models, represented by Equations (6) and (7) respectively.

The PFO kinetic model is represented by the following equation:

$$\log(q_e - q_t) = \log q_e - \frac{K_1}{2.303}\,t \tag{6}$$

where q_e and q_t (both measured in mg/g) represent the amounts of heavy metals and steroid hormones adsorbed at equilibrium and at time (t), respectively. (K_1) denotes the first-order rate constant.

The PSO kinetic model is expressed as follows:

$$\frac{t}{q_t} = \frac{1}{K_2 q_e^2} + \frac{1}{q_e}t \tag{7}$$

where K_2 represents the second-order rate constant.

Regarding the Gibbs free energy change (ΔG), entropy change (ΔS), and enthalpy change (ΔH), these parameters characterize the thermodynamics of a system [61].

$$\ln K_d = \frac{\Delta S}{R} - \frac{\Delta H}{RT} \tag{8}$$

where T is the temperature, R is the gas constant, and K_d is the distribution constant.

$$K_d = \left(\frac{C_o - C_e}{Ce}\right) \times \frac{V}{m} \tag{9}$$

where Ce (mgL^{-1}) is the equilibrium concentrations of heavy metals and steroid hormones, Co (mgL^{-1}) is the initial of heavy metals and steroid hormones, V is the volume of solution in litres (L), and m is the adsorbent mass in grams (g).

The Gibb's free energy change for respective adsorption processes was obtained from Eq. (10)

$$\Delta G = -RT\ln K_d \tag{10}$$

2.6. Investigation of leaching effect by TCLP

The leaching effect of the ball-milled iron-based MOF/biochar nanocomposite (50% FeBTC-BC) was investigated by a slightly modified toxicity characteristic leaching procedure (TCLP) method as reported by [62] and [63]. The extractant solution was prepared by the addition of 10 mL of 1N NaOH and 50 mL of glacial acetic acid into a 1 L conical flask. The solution pH was adjusted and kept at pH 5 and further dilution was done by adding 500 mL of deionized water into the conical flask. Thereafter, 25 mg of 50% FeBTC-BC was added slowly using a magnetic stirrer at 30 rpm for 18h. After stirring, the solution was then allowed to settle for 8 h, then filtered with Whatman filter paper and stored for 10 days for FTIR analysis to determine the extent of leaching of the 50% FeBTC-BC in the solution.

2.7. Reusability experiments

To assess the regeneration of the 50% FeBTC-BC adsorbent, experiments involving adsorption and desorption were conducted. The used 50% FeBTC-BC, previously employed for removing six steroid hormones (testosterone, progesterone, estriol, α-estradiol, β-estradiol, and Bisphenol A) and heavy metals (lead, nickel, and cadmium), underwent rinsing with 10 mL of ethanol solution and 10 mL of deionized water at room temperature. Following desorption, the adsorbent was filtered and dried at 353 K for reuse. The recycled ball-milled biochar was then added to 25 mL of 2 mg/L mixed solutions of the steroid hormones in each cycle of the adsorption–desorption test, which was repeated five times to evaluate the adsorption efficiency of the regenerated ball-milled biochar [64].

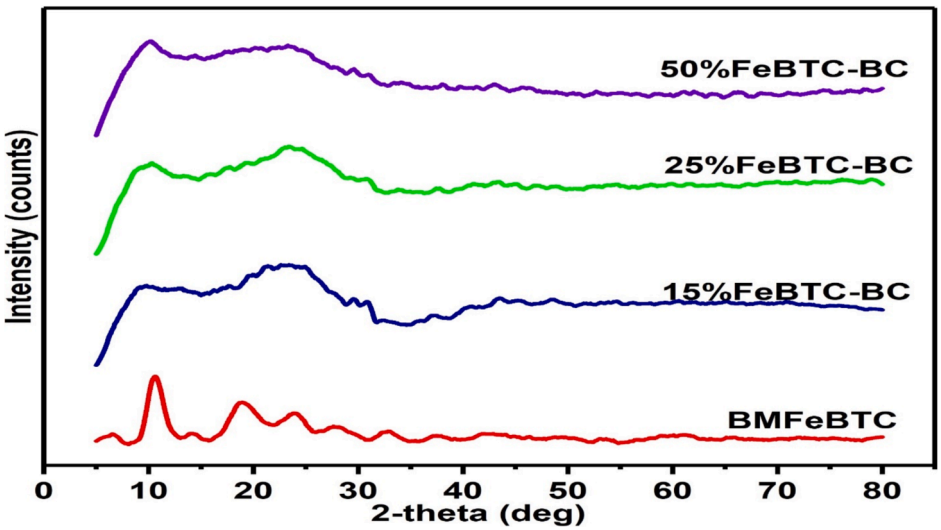

Fig. 2. XRD spectra of BMFe-BTC, 15% FeBTC-BC, 25% FeBTC-BC, and 50% FeBTC-BC.

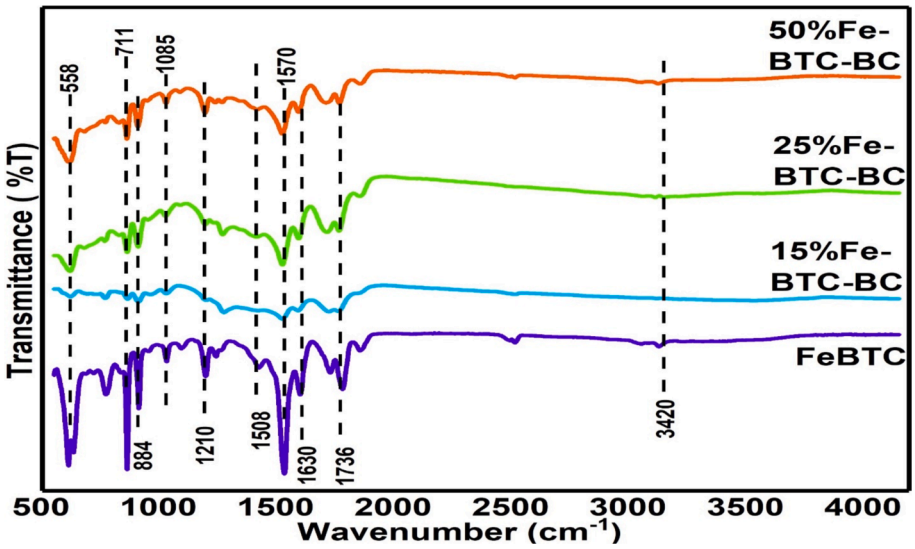

Fig. 3. FTIR spectra of Fe-BTC, 15% FeBTC-BC, 25% FeBTC-BC and 50% FeBTC-BC.

3. Result and discussion

3.1. Characterisation of biochar/MOF nanocomposites

3.1.1. BET of the biochar/MOF nanocomposites

Table 1 discloses the surface area, pore size, and grain size of the pristine biochar, ball-milled biochar, and Fe-BTC-biochar nanocomposites as determined by BET analysis. The surface area of the biochar escalated from 172 m^2g^{-1} for ASA550 to 302 m^2g^{-1} for BASA550, suggesting that the ball-milling process amplified the surface area. The surface area of the ball-milled Fe-BTC (BMFe-BTC) was quantified at 146 m^2g^{-1}, which was less than that of both the pristine and ball-milled biochar. However, the surface area of 50% FeBTC-BC was 284 m^2g^{-1}, like pure biochar. This suggests that the ball milling of Fe-BTC nanoparticles altered the surface area and porosity of the biochar composite. Moreover, it indicates that the pores on the biochar surface might have been blocked by some Fe-BTC nanoparticles, leading to a fall in the total specific surface area (SSA) of the nanocomposite. This illustrates that reducing the granular particle size increased their external surface area and altering their inner pore structure affected their interior surface area [56]. During the ball milling process, both biochar and Fe-BTC were fragmented into diminutive particles, resulting in an augmentation of the biochar's surface area and the emergence of newly formed pores and fissures. Both Fe-BTC and biochar were reduced in size during the ball milling process, which gave biochar a larger surface area and newly created fissures and holes. At the nanoscale, the Fe-BTC exhibits a high tendency to hot-extrude into the pores and fissures of biochar [65].

3.1.2. XRD analysis

Fig. 2 presents the XRD patterns of composites consisting of biochar (BC) and metal–organic frameworks (MOFs) in varying proportions. Peaks at 11.5°, 20.3°, and 27° are characteristic of the Fe-BTC structure, confirming its presence in the composites. Notably, the high purity of the Fe_2O_3 phase is indicated by the absence of its typical peaks in the patterns. When Fe-BTC is functionalized with BC and subjected to ball milling, a significant transformation occurs in its crystalline structure. The peak at 11° becomes indistinct due to the deformation of the Fe-BTC crystals caused by the high-energy impacts of the moving balls within the milling chamber, coupled with the inherent structural features of biochar. This mechanical action results in a notable reduction in crystallinity. The XRD spectra of the FeBTC-BC composites reveal broader

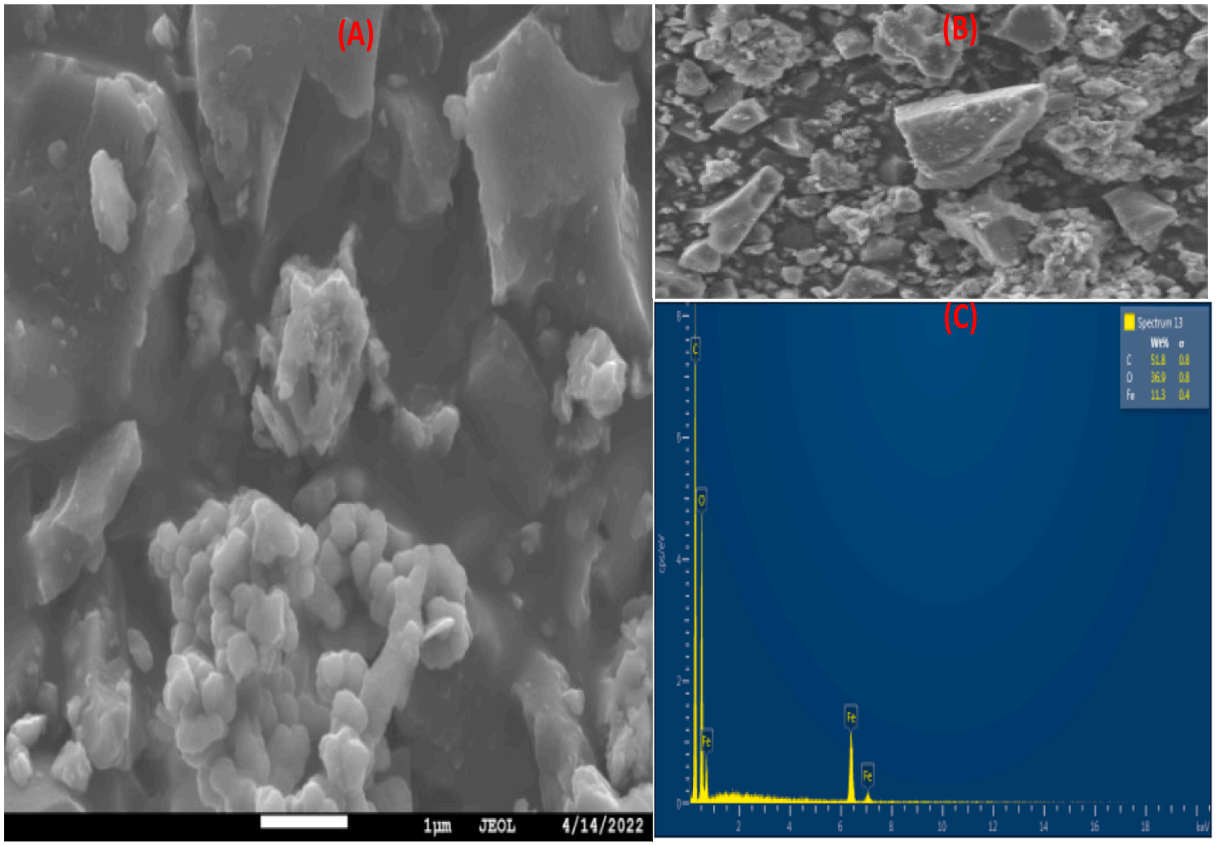

Fig. 4. (A) SEM image of 50% FeBTC-BC, (B) and (C) EDS scanning of C, Fe, and O.

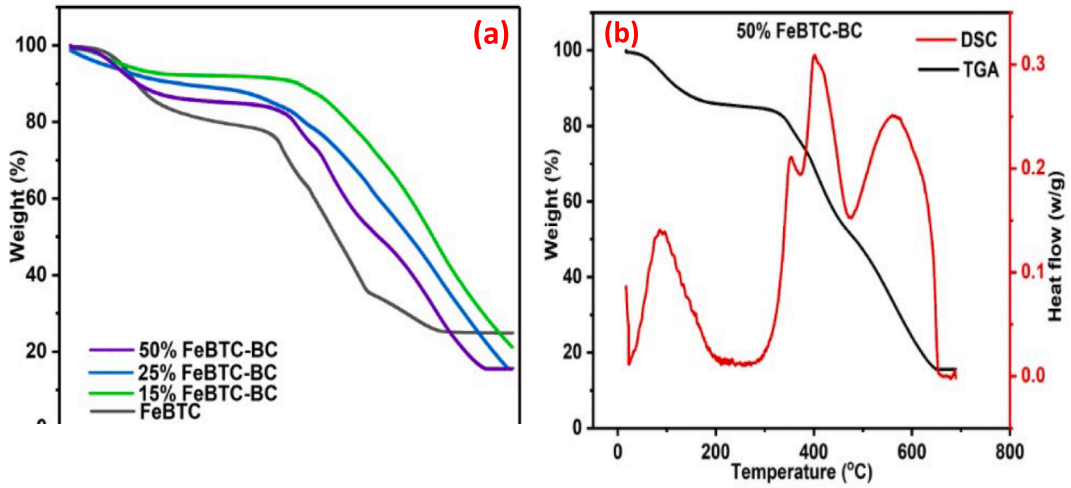

Fig. 5. TGA /DSC results of the ball-milled biochar.

reflections within the 2θ range of 20° to 30°, highlighting a decrease in crystallinity compared to pure Fe-BTC. This observation aligns with findings by [66,67], that pure Fe-BTC exhibits higher crystallinity than its composites. The amorphous nature of the 50% FeBTC-BC nanocomposite is further corroborated by the SEM-EDS analysis displayed in Fig. 4, confirming the structural changes induced by the functionalization and milling process.

3.1.3. FTIR analysis

Fig. 3 illustrates the FTIR spectra for FeBTC-BC and Fe-BTC synthesized at different percentages, providing detailed insights into the functional groups present in the materials. The absorption bands observed at 1,736 cm^{-1} and 1,630 cm^{-1} correspond to the carboxylic acid groups, specifically the vibrations of C=O bonds, which are key indicators of the functional groups in the structure. The broad band at 3,420 cm^{-1} is attributed to the stretching vibrations of –OH groups, which are present both in water molecules and as part of the metal–organic framework (MOF) ligands. This indicates the hydrophilic nature of the material and the presence of hydroxyl functionalities. Prominent peaks at 1,423 cm^{-1} and 1,570 cm^{-1} are assigned to the vibrations of C-C bonds and C=O groups, respectively, reflecting the aromatic and carbonyl features of the framework. Additionally, the

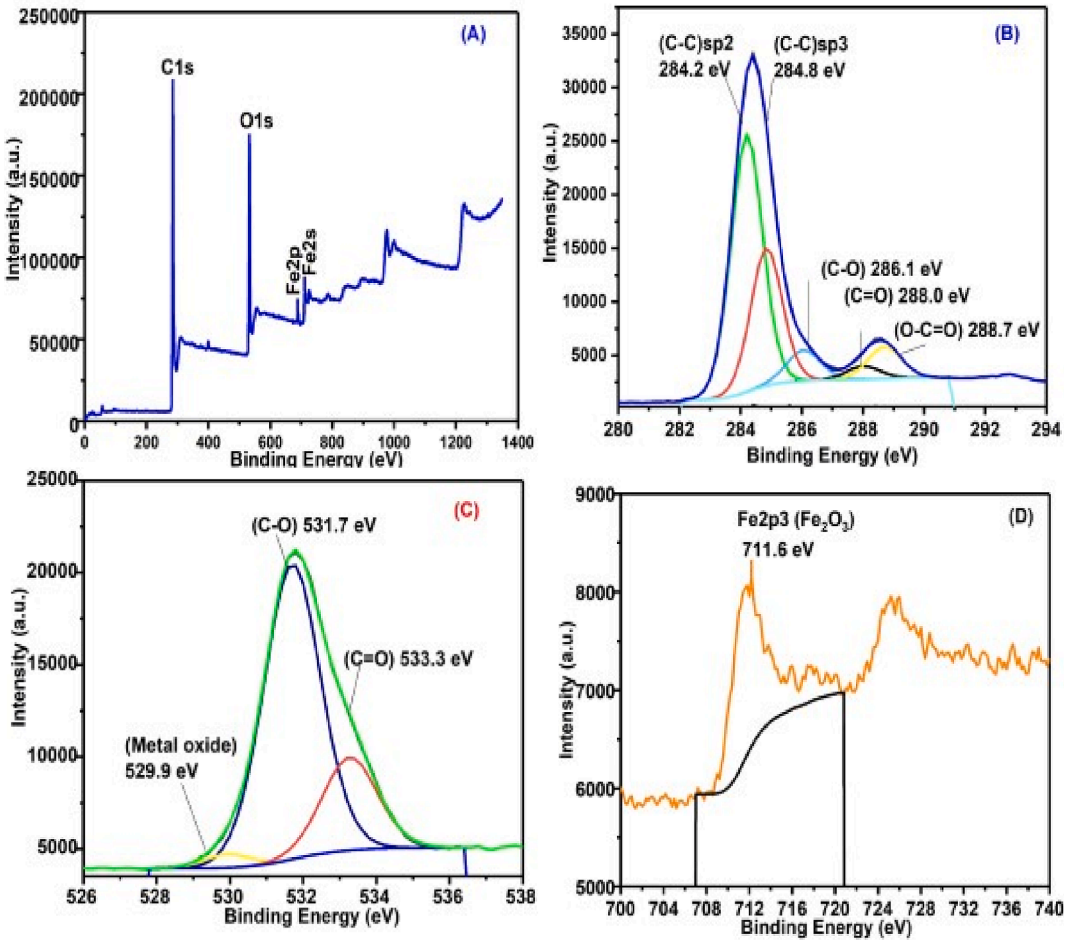

Fig. 6. XPS spectra of 50% FeBTC-BC: (a) using a complete survey scan; (b) using carbon; (c) using oxygen; and (d) using Fe scanning.

FeBTC-BC composite exhibits a distinct peak at 1,085 cm^{-1}, indicative of the C-O stretching vibrations, which are commonly associated with oxygen-containing functional groups. The spectra also reveal peaks at 759 cm^{-1} and 711 cm^{-1}, corresponding to the vibrations of C-H groups, highlighting the presence of aromatic hydrocarbons in the material. Furthermore, absorption bands at 634 cm^{-1} and 538 cm^{-1} are ascribed to Fe-O bond vibrations, confirming the incorporation of iron within the framework, consistent with findings by [66]. These spectral features collectively validate the structural integrity and functionalization of FeBTC-BC and Fe-BTC composites, as supported by [68].

3.1.4. SEM-EDS analyses 50% FeBTC-BC nanocomposite

Fig. 4 presents the SEM image of the 50% FeBTC-BC nanocomposite, captured using a JEOL JSM-IT 300 scanning electron microscope (SEM) equipped with an Oxford Instruments energy-dispersive spectroscopy (EDS) system, operating at a 20 kV electron acceleration voltage. This advanced imaging technique was employed to analyze the surface morphology and elemental composition of the composite material. In Fig. 4(A), the SEM image highlights the microstructural features of the 50% FeBTC-BC nanocomposite, showcasing its texture and uniform surface, which is indicative of effective synthesis and integration of the composite components. The accompanying EDS analysis confirmed the elemental composition of the nanocomposite, with carbon (C), iron (Fe), and oxygen (O) present at 51.8%, 36.9%, and 11.3%, respectively. These values validate the successful formation of the 50% FeBTC-BC composite by accurately combining biochar (BC) with Fe-BTC. Additionally, Fig. 4 (C) demonstrates the EDS elemental mapping, providing a visual representation of the homogeneous distribution of Fe-BTC within the biochar matrix. This uniform dispersion is crucial for ensuring consistent performance and functionality of the composite material in its intended applications. The results confirm the effective synthesis process and the compatibility of Fe-BTC and BC in forming a well-integrated nanocomposite.

3.1.5. TGA and DSC analysis

Fig. 5(a) displays the TGA (thermogravimetric analysis) curves, which provide insights into the thermal characteristics of biochar (BC) and FeBTC-BC composites at varying compositions (Fe-BTC, 15% FeBTC-BC, 25% FeBTC-BC, and 50% FeBTC-BC). The weight loss patterns observed in these curves demonstrate the disintegration behaviours of the materials under heat. The analysis reveals that incorporating biochar (BC) into the Fe-BTC matrix enhances the thermal stability of the composites, with higher percentages of biochar contributing to improved stability. This increase in thermal resistance is attributed to the higher carbon content in biochar, which imparts robustness to the composite material. In the TGA curves, the initial drop in weight between 0°C and 100°C corresponds to the evaporation of moisture and the loss of heat-labile inorganic materials. Following this, further disintegration at higher temperatures is associated with the breakdown of lignocellulosic components within the biochar. This decomposition reflects the structural changes occurring as the material is subjected to increased thermal stress. Fig. 5(b) presents the DSC (differential scanning calorimetry) curve of the 50% FeBTC-BC composite, showcasing its heat flow characteristics. Four distinct exothermic peaks are observed, indicating various thermal events, such as phase changes or chemical reactions. The data confirms that the 50% FeBTC-BC composite remains

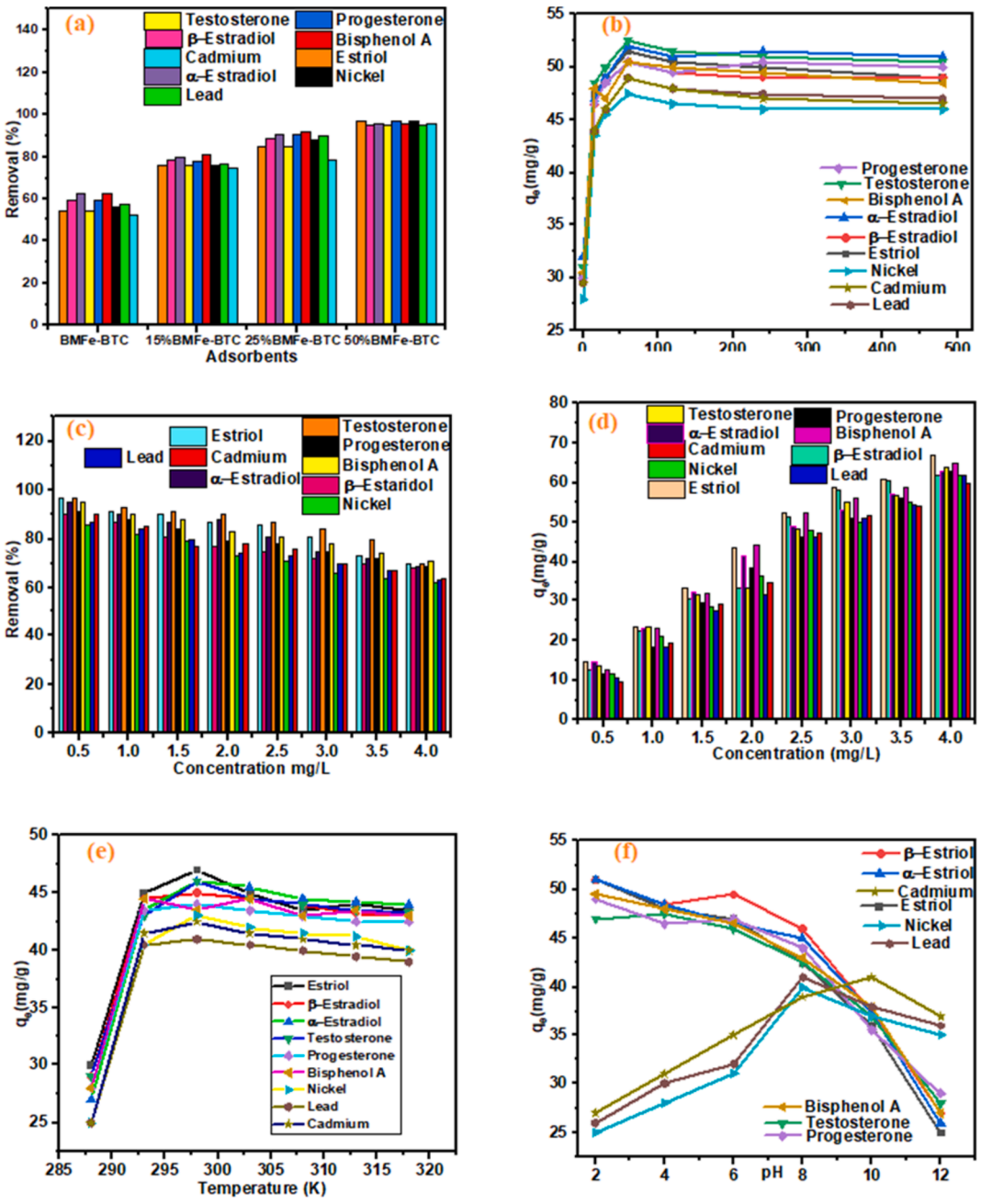

Fig. 7. (a) Type of adsorbent; (b) contact time; (c) and (d) Concentration effect on the removal; (e) temperature effect on the removal, and (f) pH effect that influence on the adsorption process and provide insights into optimizing conditions for efficient removal of steroid hormones using 50 %BMFe-BTC as the adsorbent.

Table 2
Langmuir and Freundlich adsorption isotherm values.

		Langmuir			Freundlich		
Heavy Metals	**q_{max} (mg/g)**	**K_L (L/mg)**	**R_L**	**R^2**	**K_F (mg^{-1})**	**1/n**	**R^2**
Nickel	74.18	10.71	0.0360	0.9449	27.43	0.4930	0.9775
Cadmium	85.69	3.14	0.1130	0.9654	28.00	0.5118	0.9819
Lead	82.71	4.17	0.0853	0.9447	25.46	0.4659	0.9913
Estriol	83.33	4.13	0.0883	0.9862	22.68	0.4213	0.9855
α-Estradiol	80.64	5.91	0.0634	0.9340	29.23	0.5434	0.9838
β-Estradiol	72.99	7.61	0.0499	0.9738	28.75	0.5116	0.9876
Testosterone	75.59	2.83	0.1238	0.9798	28.47	0.5485	0.9813
Progesterone	86.21	3.31	0.1078	0.9239	27.58	0.5353	0.9579
Bisphenol A	72.99	2.24	0.1515	0.9388	29.03	0.5532	0.9856

Table 3
Kinetic parameter values.

	Pseudo-first order			Pseudo-second order		
Metal	**q_e (mg/g)**	**K_1**	**R^2**	**q_e**	**K_2**	**R^2**
Nickel	1.21	0.002372	0.8932	44.19	0.0146	0.9997
Cadmium	1.22	0.002326	0.8719	42.74	0.0678	0.9995
Lead	1.23	0.002372	0.9109	40.98	0.0102	0.9985
Estriol	1.24	0.002191	0.8908	43.22	0.0067	0.9991
α-Estradiol	1.21	0.002395	0.9119	44.07	0.0071	0.9991
β- Estradiol	1.22	0.002349	0.9090	44.09	0.0121	0.9993
Testosterone	1.22	0.002372	0.8860	42.05	0.0060	0.9990
Progesterone	1.21	0.002349	0.8579	41.79	0.0108	0.9990
Bisphenol A	1.22	0.002372	0.9026	41.84	0.0076	0.9989

thermally stable within the experimental conditions of this study, further supporting its suitability for applications requiring high thermal resilience.

3.1.6. XPS analysis of 50% FeBTC-BC

An X-ray photoelectron spectrometer was utilized to analyse the elemental composition of the 50% FeBTC-BC nanocomposite, as depicted in Fig. 6(a). The full scan survey illustrates the XPS spectra of Fe, C, and O on the surface of the ball-milled Fe-MOF-BC nanocomposite. In Fig. 6(b), the carbon spectra exhibit the functional groups along with their corresponding binding energy peaks. The carbon peaks at 284.2 eV and 284.7 eV are indicative of sp2 and sp3 hybridized carbon bonds, respectively, within graphitic or amorphous carbon structures. Furthermore, the peak at 288.0 eV signifies sp2 hybridized carbon bonds in carbonyl (C=O) functionalities, while the peak at 288.7 eV is attributed to the presence of carboxyl (–COOH) groups [69]. In the oxygen (O 1s) spectra as shown in Fig. 6(c), three distinct peaks are discernible. The first peak, at 529.6 eV, is potentially linked to the metal oxide of iron (Fe) in Fe-BTC. The second peak, situated at 531.1 eV, is associated with carbonyl oxygen within carboxyl (–COOH) groups. The third peak, at 532.7 eV, is indicative of hydroxyl (–OH) groups. This observation suggests a potential explanation: the oxygen oxidation in conjunction with iron in the Fe-BTC during the ball milling process [70]. In the oxygen (O 1s) spectra depicted in Fig. 6(c), three distinct peaks are observable. The first peak, occurring at 529.6 eV, is likely associated with the metal oxide of iron (Fe) in Fe-BTC. The second peak, at 531.1 eV, corresponds to carbonyl oxygen present in carboxyl (–COOH) groups. Lastly, the third peak at 532.7 eV represents hydroxyl (–OH) groups. This observation suggests a potential explanation: the oxygen oxidation in conjunction with Fe in the Fe-BTC during the ball milling process.

4. Results of and discussion

The study explored the efficacy of various metal–organic framework (MOF)-biochar composites, prepared through ball milling, in removing heavy metals and steroid hormones from aqueous solutions. The composites, designated as BMFe-BTC, 15%BMFe-BTC, 25%BMFe-BTC, and 50%BMFe-BTC, were assessed for their ability to adsorb nickel (Ni), lead (Pb), cadmium (Cd), and steroid hormones including estriol, α-estradiol, β-estradiol, testosterone, progesterone, and Bisphenol A. The results, depicted in Fig. 7(a), revealed that the removal efficiency increased with the higher percentage of MOF in the composites. For instance, 50% BMFe-BTC exhibited the highest removal rates for Ni, Pb, and Cd at 97%, 95%, and 96%, respectively, and for the steroid hormones at percentages ranging from 95% to 97%. The rate of the removal process was also studied by varying the contact time. The data in Fig. 7(b) showed that the adsorption capacity of 50%BMFe-BTC increased with time, reaching a plateau at 60 min, which was identified as the optimal contact time. At this point, 50%BMFe-BTC demonstrated the highest adsorption capacities for the steroid hormones and heavy metals, ranging from 50.5 mg/g to 52.5 mg/g. The influence of the initial concentration of the heavy metals and steroid hormones on the adsorption process was examined by varying the concentration from 0.5 mg/L to 4 mg/L, as shown in Fig. 7 (c) and 7(d). The findings indicated that lower concentrations favoured higher removal percentages due to the presence of possible active sites on the adsorbent surface. However, as the concentration increased, the removal percentage decreased, due to the saturation of active sites. Despite this, the actual amount of adsorbate adsorbed per unit mass of the adsorbent increased with concentration. The effect of temperature on the adsorption process was assessed to determine the nature of the adsorption mechanism. As illustrated in Fig. 7(e), the adsorption capacity of 50%BMFe-BTC increased with temperature up to an optimal point at 298 K, suggesting that higher temperatures may facilitate the breaking of bonds and increase the number of active sites available for adsorption, thereby enhancing the adsorption capacities.

Finaly, the investigation into the influence of pH on the adsorption capabilities of 50%BMFe-BTC was conducted across a pH spectrum from 2 to 12. The findings, presented in Fig. 7(f), indicate that the adsorption capacity of 50%BMFe-BTC for heavy metals was at its nadir within the acidic pH range. This phenomenon can be ascribed to the abundance of hydrogen ions (H^+) in the acidic environment, which may confer a positive charge to the surface of 50%BMFe-BTC. Since heavy metal ions ($Ni^{2+,}$ $Cd^{2+,}$ and $Pb^{2+)}$ are also positively charged, this scenario could lead to electrostatic repulsion, thereby impeding the adsorption of these ions onto the composite surface. As the pH was incrementally raised from 2 to 6, a concomitant increase in adsorption capacities was observed, culminating in a maximum at pH 8. This trend can be explained by the increasing prevalence of hydroxyl ions (OH–) in the solution, which may induce a negative charge on the surface of 50% BMFe-BTC. The negatively charged surface would then exhibit an affinity for the positively charged metal ions, facilitating their adsorption into the porous structure of the composite. However, beyond pH 8, a decline in adsorption capacity was noted. This decrease can be attributed to the precipitation of heavy metal ions in the highly alkaline solution, which hampers the adsorption process. In contrast, the removal efficiency of 50%BMFe-BTC for steroid hormones exhibited a different pH-dependent behaviour. As depicted in Fig. 7(f), the efficiency diminished in the basic pH range. This variation could be linked to changes in the chemical forms of steroid hormones at different pH levels and potential modifications in the surface charge of 50%BMFe-BTC. The optimal removal efficiency for steroid hormones was attained at lower pH values, ranging from 2 to 6.

4.1. Adsorption isotherm studies

The empirical adsorption data exhibited a commendable alignment with both the Freundlich and Langmuir adsorption isotherm models, as illustrated in Fig. S1(a)-(b) and Fig. S1(c)-(d) (supplementary data), respectively. The high coefficient of correlation (R^2) values obtained for both models—Langmuir (R^2 = 0.9239 – 0.9862) and Freundlich (R^2 = 0.9579 – 0.9913)—signify a robust concordance with the experimental data, as delineated in Table 2. This indicates that both the Freundlich and Langmuir isotherm models adeptly encapsulate the adsorption process. Upon comparing the R^2 values, the Freundlich isotherm model demonstrated a superior fit, as evidenced in Table 2.

In the present investigation, the dimensionless separation factor (R_L) for all the heavy metals and steroid hormones spanned a range from 0.0523 to 0.2074, which falls within the interval of 0 to 1, thereby implying a favourable Langmuir adsorption process. An R_L value of 0 denotes irreversible adsorption, while values between 0 and 1 indicate favourable adsorption conditions. An R_L value equal to 1 suggests linear adsorption, and values exceeding 1 are considered indicative of unfavourable adsorption. The Langmuir isotherm analysis yielded maximum adsorption capacities (q_{max} (mgg^{-1})) of 74.18, 82.71, and 85.69 mgg^{-1}

Table 4
Thermodynamics parameter values.

Contaminant	Temperature (K)	K_d	Ln (K_d)	ΔG ($KJmol^{-1}$)	ΔH (KJ/mol)	ΔS ($Jmol^{-1}K^{-1}$)	R^2
Nickel	288	22	3.09	−7326.96	92.20	60.31	0.9911
	293	38.5	3.65	−8891.40			
	298	41	3.71	−9191.79			
	303	40	3.69	−9295.69			
	308	39.5	3.68	−9423.42			
	313	39.25	3.67	−9550.37			
	318	38	3.64	−9623.62			
Cadmium	288	23	3.14	−7518.52	87.34	53.60	0.9920
	293	39.5	3.69	−8988.84			
	298	40.5	3.70	−9167.02			
	303	39.5	3.68	−9270.44			
	308	39	3.66	−9372.21			
	313	38.5	3.65	−9493.33			
	318	38	3.64	−9650.06			
Lead	288	23	3.14	−7518.51	77.94	55.49	0.9918
	293	38.5	3.65	−8891.40			
	298	39	3.66	−9067.91			
	303	38.5	3.65	−9194.87			
	308	38	3.63	−9295.38			
	313	37.5	3.62	−9420.26			
	318	37.5	3.62	−9570.74			
Estriol	288	27	3.30	−7901.63	62.62	51.21	0.9960
	293	42	3.74	−9110.64			
	298	44	3.78	−9365.22			
	303	42	3.74	−9421.59			
	308	41.5	3.73	−9551.46			
	313	41	3.71	−9654.47			
	318	40.5	3.70	−9782.25			
α-Estradiol	288	24	3.18	−7614.30	90.16	60.13	0.9924
	293	40.5	3.70	−9013.20			
	298	43	3.76	−9315.67			
	303	42.5	3.75	−9446.78			
	308	41.5	3.73	−9551.46			
	313	41.25	3.72	−9680.49			
	318	41	3.71	−9808.69			
β-Estradiol	288	26	3.26	−7805.85	67.94	52.78	0.9957
	293	41.5	3.73	−9086.29			
	298	42	3.74	−9266.12			
	303	41.5	3.73	−9396.40			
	308	41	3.71	−9500.24			
	313	40.25	3.70	−9628.44			
	318	40	3.69	−9755.81			
Testosterone	288	26	3.29	−7877.68	72.38	54.26	0.9925
	293	40	3.69	−8988.85			
	298	43	3.76	−9142.24			
	303	41.5	3.73	−9396.40			
	308	41	3.71	−9500.24			
	313	40.5	3.70	−9628.44			
	318	40.25	3.69	−9755.81			
Progesterone	288	25	3.22	−7710.07	72.88	54.21	0.9946
	293	40.5	3.70	−9013.21			
	298	41	3.71	−9191.79			
	303	40.5	3.70	−9320.83			
	308	40	3.69	−9449.03			
	313	39.5	3.68	−9576.40			
	318	39.5	3.68	−9729.38			
Bisphenol A	288	25	3.22	−7710.07	73.17	54.46	0.9948
	293	41.5	3.73	−7843.93			
	298	42.5	3.75	−9290.90			
	303	41.5	3.73	−9396.39			
	308	40	3.69	−9449.02			
	313	40.5	3.70	−9628.44			
	318	40	3.69	−9755.81			

for nickel (Ni), lead (Pb), and cadmium (Cd), respectively. In a similar vein, the Freundlich isotherm analysis revealed maximum adsorption capacities (K_f (mgg^{-1})) of 27.43, 25.46, and 28.00 mgg^{-1} for Ni, Pb, and Cd, respectively. With respect to steroidal hormones, the Langmuir isotherm analysis furnished maximum adsorption capacities of 75.59, 86.21, 80.64, 83.33, 72.99, and 72.99 mgg^{-1} for testosterone, progesterone, α-estradiol, estriol, Bisphenol A and β-estradiol, respectively. Conversely, the Freundlich isotherm analysis yielded maximum adsorption capacities of 28.47, 27.58, 22.68, 29.23, 28.75, and 29.03 mgg^{-1} for the steroidal hormones and Bisphenol A, respectively. The favourable values of $K_f > 1$ derived from the Freundlich isotherm model suggest that the adsorption process is predisposed towards the extraction of steroidal hormones and heavy metals via multilayer physicochemical adsorption on a heterogeneous surface.

4.2. Kinetic studies

The analysis of the experimental data via the application of the

Table 5
Steroid hormone and heavy metal removal efficiency of biochar-MOF nanocomposite in ultrapure water and real wastewater sample.

Analytes	Ultrapure water (% removal)	Effluent (% removal)	Influent (% removal)
Estriol	91	88	86
α-Estradiol	88	85	80
β-Estradiol	93	84	77
Testosterone	87	80	79
Progesterone	90	87	78
Bisphenol A	92	85	79
Nickel	93	89	77
Cadmium	92	88	84
Lead	94	89	85

Pseudo-First order (PFO) and Pseudo-Second order (PSO) kinetic models provided insight into the temporal aspects of the adsorption process, as illustrated in Fig. S2a and S2b (Supplementary data). The analysis indicated that the PSO kinetic model, which suggests that the rate-limiting step involves chemical sorption or chemisorption, yielded a linear plot, as depicted in Fig. S2(b).

Upon comparing the two kinetic models, it was evident that the PSO model provided a more precise depiction of the adsorption process. This determination was based on the coefficients of determination (R^2) for both models, which ranged from 0.8579 to 0.9119 for the PFO model and from 0.9985 to 0.9997 for the PSO model, as detailed in Table 3. The results suggest that the PSO kinetics is the rate-limiting step, indicating that the interaction could involve chemical sorption or chemisorption.

4.3. Thermodynamics studies

It is imperative to confirm if an adsorption process is spontaneous and feasible, this requires the utilization of thermodynamic parameters. Table 4 lists the values of ΔG, which were determined using Eq. (11) at different temperatures. The removal of metals ions and steroid hormones on the surface of 50% FeBTC-BC is an endothermic process, as indicated by the positive value of ΔH. In accordance with Crini *et al.*, [71], chemisorption is the mode of adsorption if is more than 40 kJ/mol. In addition, the positive values of ΔH confirmed that a chemical interaction was responsible for the heavy metals and steroid hormones adsorption on 50% FeBTC-BC. Adsorption of metal ions and steroidal hormones on the adsorbent surface was found to be spontaneous and thermodynamically advantageous, as shown by the negative values of ΔG across all temperature ranges. As indicated in Table 4, the value of

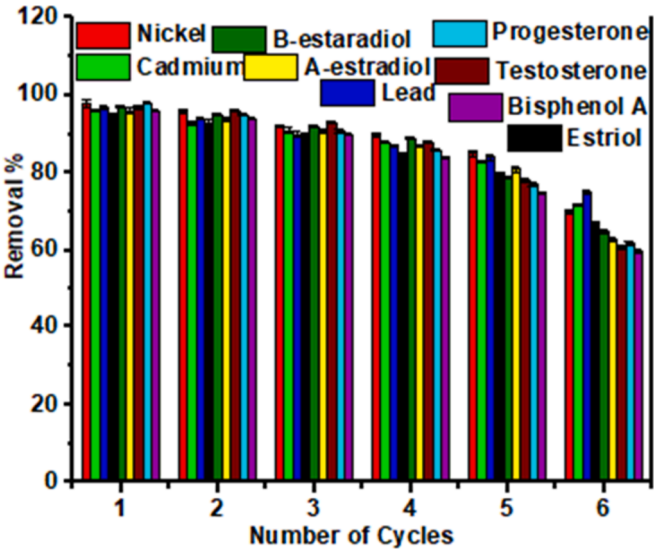

Fig. 9. Reusability of 50% FeBTC-BC regenerated by ethanol indicating the removal efficiency for steroid hormones and heavy metals.

ΔG decreases with an increase in temperature, suggesting that elevated temperatures (318 K) are more conducive to the adsorption of both heavy metals and steroid hormones onto the adsorbent. The positive value of ΔS reflects the enhancement in randomness at the solid/solution interface, which is a consequence of the binding of metal ions and steroidal hormones to the active sites of the adsorbent [72].

5. Application of biochar-MOF nanocomposite for the elimination of mixed steroid hormones and heavy metals from wastewater

The efficacy of the ball-milled biochar-MOF nanocomposite was assessed for the simultaneous extraction of heavy metals and steroid hormones from authentic wastewater samples sourced from a wastewater treatment facility. The findings, outlined in Table 5, demonstrate the effectiveness of the adsorbent in removing both steroid hormones and heavy metals from the wastewater sample. Specifically, the highest removal percentages for steroid hormones in wastewater and deionized (DI) water were observed to be 86%, 88%, and 93% for effluent, influent, and DI water mixed solution, respectively. Similarly, for mixed

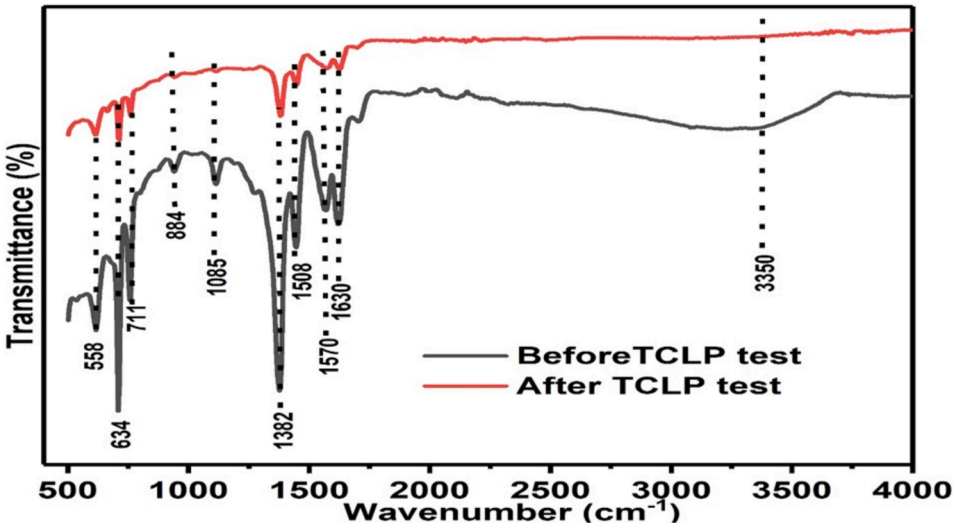

Fig. 8. FTIR spectra of the FeBTC-BC nanocomposite before and after the leaching experiment.

Table 6
Comparison of reported research and the current work on biochar-based composites for the removal of organic pollutants and heavy metals.

Biochar-based composite	Pollutant	% removal	Reference
Sugar beet-MgO	NO_3^- and PO_4^{3-}	66 and 11	[74]
Bamboo-Chitosan	Pb	35	[75]
Rice Husk-Ca	As^{5+}	70 enhanced	[76]
Gumwood-CNT/GO	Cd and Pb	Higher enhanced	[77]
Corncobs-Mn	Pb	99	[78]
Macroalgal biomass-FeCl	Molybdenum	78	[79]
Macroalgal biomass-FeCl	Arsenic	60	[79]
Macroalgal biomass-FeCl	Selenium	38	[79]
Potato stem- Attapulgite	Norfloxacin	80	[80]
Eucalyptus- nZVI	Chloramphenicol	72	[81]
Carbon-MOF-derived	BPA	49	[82]
Biochar-SiO_2/CNTs	EE2	65	[83]
African star apple-MOFs	Pb	85–89	Present study
African star apple-MOFs	Cd	84–88	Present study
African star apple-MOFs	Ni	77–89	Present study
African star apple-MOFs	BPA	79–85	Present study
African star apple-MOFs	Estriol	86–88	Present study
African star apple-MOFs	Progesterone	78–87	Present study
African star apple-MOFs	Testosterone	79–80	Present study
African star apple-MOFs	Alpha Estradiol	80–85	Present study
African star apple-MOFs	Beta Estradiol	77–84	Present study

heavy metals solutions, removal percentages of 89%, 85%, and 94% were attained for effluent, influent, and DI water mixed solutions, respectively.

5.1. Result of the leaching experiment for FeBTC-BC test by TCLP trials

The results obtained from the toxicity characteristic leaching procedure (TCLP) test showed that 2.58 mg of Fe-BTC leached out of the precipitated residue left behind from the 25 mg FeBTC-BC nanocomposite at an extreme condition of pH 5. Furthermore, FTIR analysis was used to confirm the stability of the FeBTC-BC nanocomposite before and after the leaching experiment as shown in Fig. 8. Comparing the two spectra, it can be seen clearly that the functional groups were present at their respective wavelengths in the spectra before and after the TCLP test, although differences in their respective peaks were observed which could be attributed to the wash-out during the TCLP experiment. Consequently, from the FTIR result, no significant differences were found between the spectra of FeBTC-BC before and after the TCLP experiment [62].

5.2. Reusability of the 50% FeBTC-BC

Adsorbent reusability is crucial for an economical approach to long-term pollution removal. The adsorption performance of 50% FeBTC-BC that has been regenerated is shown in Fig. 9. As Fig. 9 illustrates, the adsorption capability of regenerated 50% FeBTC-BC decreased gradually. Only after the fifth cycle did the 50% FeBTC-BC adsorption ability fall noticeably below 60% after the 5th cycles. The depletion of functional groups present on the surface of the 50% FeBTC-BC is responsible for the 50% FeBTC-BC's decreased adsorption capability following each desorption experiment. These experimental results demonstrated the possibility of five reuses for the 50% FeBTC-BC adsorbent. Comparing these results with the reusability results obtained in our recent research where ball-milled modified biochar was used, this shows that ball-milled biochar-MOFs composite has more regeneration efficiency than the ball-milled biochar with good efficiency for the first 4th cycles [73].

5.3. Mechanisms of biochar-MOF composite

The biochar-MOF nanocomposites facilitate the elimination of lead (Pb), nickel (Ni), and cadmium (Cd) via a complex interplay of mechanisms. These encompass cation exchange, mediated by exchangeable sites on the biochar's surface, interactions with oxygen-containing functional groups within carbon-based nanomaterials, electrostatic forces, and surface adsorption onto both carbon nanomaterials and biochar surfaces [84 85]. Earlier studies have shown that carboxyl (–COOH) and hydroxyl (–OH) groups, which are found in graphene oxide (GO) and chemically modified carbon nanotubes (CNTs), can create strong complexes with Pb, Ni, and Cd in water [86,87]. Additionally, the mechanism by which steroid hormones are adsorbed onto biochar-MOF nanocomposites may involve π-π interactions, which stem from the connection between aromatic rings. The adsorption capability of metal–organic frameworks (MOFs) within the biochar-MOF nanocomposites, however, can be ascribed to the formation of stacking interactions between the steroid hormones and the MOFs. Previous research has documented analogous mechanisms between MOFs and organic pollutants. For example, investigations into ZIF-8 by Abdi et al. revealed that the aromatic ring can engage with the crew in malachite green, leading to an enhanced removal capacity through π-π interaction [88]. Chen et al. explored the adsorption mechanism of Congo Red using Co-MOFs and reported that π-π interactions can be activated between the dye and Co-MOF by exposing an active metal site. The MOF is equipped with a benzene ring, which, like the benzene rings in Congo Red, has the potential to engage in π-π interactions [89]. The comparative findings presented in Table 6 indicate that the removal efficacy of the synthesized composite material substantially surpasses the outcomes documented in other studies.

6. Conclusions

The study demonstrated that ball-milled biochar-metal–organic framework (MOF) composites effectively removed steroid hormones and heavy metals from wastewater and deionized (DI) water. Maximum removal efficiencies reached 86% for effluent, 88% for influent, and 93% for DI water in steroid hormone solutions, while heavy metal solutions achieved 85%, 89%, and 94%, respectively. Adsorption efficiency was influenced by pH, contact time, and initial contaminant concentration. The Freundlich isotherm best described the adsorption process, and pseudo-second-order kinetics accurately modelled the adsorption rate. Thermodynamic analysis showed the process to be endothermic and non-spontaneous. Additionally, leaching tests confirmed the stability of the biochar-MOF composite, with FTIR spectra showing no significant structural changes before and after the test. These findings highlight the potential of the FeBTC-biochar composite for efficient and stable wastewater treatment.

Consent to publish

The authors have consented to the submission of this manuscript to the journal.

CRediT authorship contribution statement

Sefiu Olaitan Amusat: Formal analysis, Data curation, Conceptualization. **Temesgen Girma Kebede:** Supervision, Project administration, Methodology, Funding acquisition. **Edward Ndumiso Nxumalo:** Writing – review & editing, Validation, Supervision. **Simiso Dube:** Supervision, Project administration. **Mathew Muzi Nindi:** Writing – review & editing, Writing – original draft, Supervision, Project administration, Funding acquisition.

Funding

TWAS-NRF Doctoral Scholarship (Grant Number 116111 and 139178).

Declaration of competing interest

The authors declare that they have no known competing financial interests or personal relationships that could have appeared to influence the work reported in this paper.

Acknowledgment

The authors express their sincere gratitude to the Chemistry Department at UNISA for providing access to all the necessary equipment required for this research project.

Appendix A. Supplementary data

Supplementary data to this article can be found online at https://doi.org/10.1016/j.rechem.2025.102050.

Data availability

No data was used for the research described in the article.

References

[1] K. Haddad, A. Gheid, D. Haddad, K. Oulmi, Experimental and numerical study on the leaching of pesticides into the groundwater through a porous medium: Effects of transport parameters, Environ. Technol. Innov. 13 (2019) 244–256.
[2] M.D. Yahya, A.S. Aliyu, K.S. Obayomi, A.G. Olugbenga, U.B. Abdullahi, Column adsorption study for the removal of chromium and manganese ions from electroplating wastewater using cashew nutshell adsorbent, Cogent Eng. 7 (2020) 1748470.
[3] R. Deng, D. Huang, J. Wan, W. Xue, X. Wen, X. Liu, S. Chen, L. Lei, Q. Zhang, Recent advances of biochar materials for typical potentially toxic elements management in aquatic environments: a review, J. Clean. Prod. 255 (2020) 119523.
[4] M.B. Shakoor, S. Ali, M. Rizwan, F. Abbas, I. Bibi, M. Riaz, U. Khalil, N.K. Niazi, J. Rinklebe, A review of biochar-based sorbents for separation of heavy metals from water, Int. J. Phytoremediation 22 (2020) 111–126.
[5] S. Saba, M.S.H. Akash, K. Rehman, U. Saleem, F. Fiayyaz, T. Ahmad, Assessment of heavy metals by ICP-OES and their impact on insulin stimulating hormone and carbohydrate metabolizing enzymes, Clin. Exp. Pharmacol. Physiol. 47 (2020) 1682–1691.
[6] S. Sabir, M.S.H. Akash, F. Fiayyaz, U. Saleem, M.H. Mehmood, K. Rehman, Role of cadmium and arsenic as endocrine disruptors in the metabolism of carbohydrates: Inserting the association into perspectives, Biomed. Pharmacother. 114 (2019) 108802.
[7] M.I. Inyang, B. Gao, Y. Yao, Y. Xue, A. Zimmerman, A. Mosa, P. Pullammanappallil, Y.S. Ok, X. Cao, A review of biochar as a low-cost adsorbent for aqueous heavy metal removal, Crit. Rev. Environ. Sci. Technol. (2016), https://doi.org/10.1080/10643389.2015.1096880.
[8] C. He, W. Xia, C. Zhou, D. Huang, C. Zhang, B. Song, Y. Yang, J. Li, X. Xu, Y. Shang, Rational design to manganese and oxygen co-doped polymeric carbon nitride for efficient nonradical activation of peroxymonosulfate and the mechanism insight, Chem. Eng. J. 430 (2022) 132751.
[9] L. Li, D. Zou, Z. Xiao, X. Zeng, L. Zhang, L. Jiang, A. Wang, D. Ge, G. Zhang, F. Liu, Biochar as a sorbent for emerging contaminants enables improvements in waste management and sustainable resource use, J. Clean. Prod. (2019), https://doi.org/10.1016/j.jclepro.2018.11.087.
[10] K. Wojnarowski, P. Podobiński, P. Cholewińska, J. Smoliński, K. Dorobisz, Impact of estrogens present in environment on health and welfare of animals, Animals 11 (2021) 2152.
[11] E. Amenyogbe, G. Chen, Z. Wang, X. Lu, M. Lin, A.Y. Lin, A review on sex steroid hormone estrogen receptors in mammals and fish, Int. J. Endocrinol. 2020 (2020) 5386193.
[12] A. Bohra, S. Bhateja, Carcinogenesis and sex hormones: a review, Endocrinol Metab Synd 4 (2015) 1017–2161.
[13] B.E. Henderson, H.S. Feigelson, Hormonal carcinogenesis, Carcinogenesis 21 (2000) 427–433.
[14] L. Li, D. Zou, Z. Xiao, X. Zeng, L. Zhang, L. Jiang, A. Wang, D. Ge, G. Zhang, F. Liu, Biochar as a sorbent for emerging contaminants enables improvements in waste management and sustainable resource use, J. Clean. Prod. 210 (2019) 1324–1342, https://doi.org/10.1016/j.jclepro.2018.11.087.
[15] Y. Tong, P.J. McNamara, B.K. Mayer, Adsorption of organic micropollutants onto biochar: a review of relevant kinetics, mechanisms and equilibrium, Environ. Sci. Water Res. Technol. 5 (2019) 821–838.
[16] A. Chavoshani, M. Hashemi, M.M. Amin, S.C. Ameta, Conclusions and future research, in: Micropollutants and Challenges, Elsevier Amsterdam, Netherlands, 2020: pp. 249–256.
[17] H. Wang, X. Yang, L. He, K. Lu, K. Müller, K. McGrouther, S. Xu, X. Zhang, J. Li, H. Huang, Using biochar for remediation of contaminated soils, Twenty Years Res. Dev. Soil Pollut. Remediat. China (2018) 763–783.
[18] A. Chavoshani, M. Hashemi, M.M. Amin, S.C. Ameta, Pharmaceuticals as emerging micropollutants in, Micropollutants Challenges Emerg. Aquat. Environ. Treat. Process. (2020) 35.
[19] N. Cheng, B. Wang, P. Wu, X. Lee, Y. Xing, M. Chen, B. Gao, Adsorption of emerging contaminants from water and wastewater by modified biochar: A review, Environ. Pollut. (2021), https://doi.org/10.1016/j.envpol.2021.116448.
[20] Y. Yao, B. Gao, H. Chen, L. Jiang, M. Inyang, A.R. Zimmerman, X. Cao, L. Yang, Y. Xue, H. Li, Adsorption of sulfamethoxazole on biochar and its impact on reclaimed water irrigation, J. Hazard. Mater. (2012), https://doi.org/10.1016/j.jhazmat.2012.01.046.
[21] M. Abhinaya, R. Parthiban, P.S. Kumar, D.-V.-N. Vo, A review on cleaner strategies for extraction of chitosan and its application in toxic pollutant removal, Environ. Res. 196 (2021) 110996.
[22] X. Tong, Y. Li, F. Zhang, X. Chen, Y. Zhao, B. Hu, X. Zhang, Adsorption of 17β-estradiol onto humic-mineral complexes and effects of temperature, pH, and bisphenol A on the adsorption process, Environ. Pollut. 254 (2019) 112924.
[23] M.S. Reid, S.A. Kedzior, M. Villalobos, E.D. Cranston, Effect of ionic strength and surface charge density on the kinetics of cellulose nanocrystal thin film swelling, Langmuir 33 (2017) 7403–7411.
[24] M. Panayotova, Removal of Cr (VI) from wastewater by silver-loaded natural clinoptilolite, in: E3S Web Conf., EDP Sciences, 2021: p. 6008.
[25] A. Gopinath, G. Divyapriya, V. Srivastava, A.R. Laiju, P.V. Nidheesh, M.S. Kumar, Conversion of sewage sludge into biochar: A potential resource in water and wastewater treatment, Environ. Res. 194 (2021) 110656.
[26] S. Hussain, M.A. Abid, K.S. Munawar, A. Saddiqa, M. Iqbal, M. Suleman, M. Hussain, M. Riaz, T. Ahmad, A. Abbas, Choice of Suitable Economic Adsorbents for the Reduction of Heavy Metal Pollution Load., Polish, J. Environ. Stud. 30 (2021).
[27] S.M. Shaheen, N.K. Niazi, N.E.E. Hassan, I. Bibi, H. Wang, D.C.W. Tsang, Y.S. Ok, N. Bolan, J. Rinklebe, Wood-based biochar for the removal of potentially toxic elements in water and wastewater: a critical review, Int. Mater. Rev. 64 (2019) 216–247, https://doi.org/10.1080/09506608.2018.1473096.
[28] S.O. Amusat, T.G. Kebede, S. Dube, M.M. Nindi, Ball-milling synthesis of biochar and biochar–based nanocomposites and prospects for removal of emerging contaminants: a review, J. Water Process Eng. 41 (2021) 101993, https://doi.org/10.1016/j.jwpe.2021.101993.
[29] M. Ahmad, A.U. Rajapaksha, J.E. Lim, M. Zhang, N. Bolan, D. Mohan, M. Vithanage, S.S. Lee, Y.S. Ok, Biochar as a sorbent for contaminant management in soil and water: a review, Chemosphere 99 (2014) 19–33.
[30] H. Lyu, S. Xia, J. Tang, Y. Zhang, B. Gao, B. Shen, Thiol-modified biochar synthesized by a facile ball-milling method for enhanced sorption of inorganic Hg2 + and organic CH3Hg+, J. Hazard. Mater. 384 (2020) 121357.
[31] A. Korus, A. Szlęk, A. Samson, Physicochemical properties of biochars prepared from raw and acetone-extracted pine wood, Fuel Process. Technol. 185 (2019) 106–116.
[32] S. Chen, Y. Yu, Response Surface Methodology for Optimization of Bisphenol A Degradation Using Fe3O4-Activated Persulfate, Catalysts 13 (2023) 128.
[33] S. Lv, C. Li, J. Mi, H. Meng, A functional activated carbon for efficient adsorption of phenol derived from pyrolysis of rice husk, KOH-activation and EDTA-4Na-modification, Appl. Surf. Sci. 510 (2020) 145425.
[34] K.-W. Jung, S.Y. Lee, Y.J. Lee, Hydrothermal synthesis of hierarchically structured birnessite-type MnO2/biochar composites for the adsorptive removal of Cu (II) from aqueous media, Bioresour. Technol. 260 (2018) 204–212.
[35] A.U. Rajapaksha, S.S. Chen, D.C.W. Tsang, M. Zhang, M. Vithanage, S. Mandal, B. Gao, N.S. Bolan, Y.S. Ok, Engineered/designer biochar for contaminant removal/immobilization from soil and water: Potential and implication of biochar modification, Chemosphere (2016), https://doi.org/10.1016/j.chemosphere.2016.01.043.
[36] M. Khan, S. Khan, M. Omar, M. Sohail, I. Ullah, Nickel and Cobalt Magnetic Nanoparticles (MNPs): Synthesis, Characterization, and Applications, J. Chem. Rev. 6 (2024) 94–114.
[37] H. Ao, W. Cao, Y. Hong, J. Wu, L. Wei, Adsorption of sulfate ion from water by zirconium oxide-modified biochar derived from pomelo peel, Sci. Total Environ. 708 (2020) 135092.
[38] J. Zhang, X. Ma, L. Yuan, D. Zhou, Comparison of adsorption behavior studies of Cd2+ by vermicompost biochar and KMnO4-modified vermicompost biochar, J. Environ. Manage. 256 (2020) 109959.
[39] K.O. Otun, X. Liu, D. Hildebrandt, Metal-organic framework (MOF)-derived catalysts for Fischer-Tropsch synthesis: Recent progress and future perspectives, J. Energy Chem. (2020), https://doi.org/10.1016/j.jechem.2020.03.062.
[40] K.O. Otun, S.O. Amusat, I.T. Bello, J. Abdulsalam, A.T. Ajiboye, A.A. Adeleke, S. O. Azeez, Recent advances in the synthesis of various analogues of MOF-based nanomaterials: A mini-review, Inorganica Chim. Acta 536 (2022) 120890.
[41] S.O. Amusat, T.G. Kebede, E.N. Nxumalo, S. Dube, M.M. Nindi, Incorporating pristine biochar into metal-organic frameworks: Facile green synthesis, characterization, and wastewater remediation, Bioresour. Technol. Reports 19 (2022) 101160.
[42] Z. Li, W. Zeng, Y. Li, Recent Progress in MOF-Based Electrochemical Sensors for Non-Enzymatic Glucose Detection, Molecules 28 (2023) 4891.
[43] V. Russo, M. Hmoudah, F. Broccoli, M.R. Iesce, Applications of Metal Organic Frameworks in Wastewater Treatment : A Review on Adsorption and Photodegradation 2 (2020) 1–13, https://doi.org/10.3389/fceng.2020.581487.

[44] S. Kitagawa, Metal–organic frameworks (MOFs), Chem. Soc. Rev. 43 (2014) 5415–5418.
[45] Z. Guo, Z. Zhang, Z. Li, M. Dou, F. Wang, Well-defined gradient Fe/Zn bimetal organic framework cylinders derived highly efficient iron-and nitrogen-codoped hierarchically porous carbon electrocatalysts towards oxygen reduction, Nano Energy 57 (2019) 108–117.
[46] R. Nivetha, P. Kollu, K. Chandar, S. Pitchaimuthu, S.K. Jeong, A.N. Grace, Role of MIL-53 (Fe)/hydrated–dehydrated MOF catalyst for electrochemical hydrogen evolution reaction (HER) in alkaline medium and photocatalysis, RSC Adv. 9 (2019) 3215–3223.
[47] J.-Q. Chen, Z. Sharifzadeh, F. Bigdeli, S. Gholizadeh, Z. Li, M.-L. Hu, A. Morsali, MOF composites as high potential materials for hazardous organic contaminants removal in aqueous environments, J. Environ. Chem. Eng. 11 (2023) 109469.
[48] O.K. Akeremale, Adsorbents for Purification of Dye-Contaminated Wastewater: A Review, J. Chem. Rev. 4 (2022).
[49] C. Hu, X. Hu, R. Li, Y. Xing, MOF derived ZnO/C nanocomposite with enhanced adsorption capacity and photocatalytic performance under sunlight, J. Hazard. Mater. 385 (2020) 121599.
[50] K.D. Alanazi, B.H. Alshammari, O.A.S. Ahmad, M.M. Aljohani, H.H. Alsharief, A. H. Al-Bagawi, A.H. Alsehli, N.M. El-Metwaly, Citric acid-cross linked with magnetic metal-organic framework composite sponge for superior adsorption of indigo carmine blue dye from aqueous solutions: Characterization and adsorption optimization via Box–Behnken design, J. Mol. Struct. 1299 (2024) 137131.
[51] Z.A. Al-Ahmed, M. Alhasani, M.M. Aljohani, R.M. Snari, H.A. Alghasham, N. M. Alatawi, A.A. Keshk, N.M. El-Metwaly, Facile synthesis of new metal-organic framework/chitosan composite sponge for Hg (II) removal: Characterization, adsorption efficiency, and optimization using Box-Behnken design, Int. J. Biol. Macromol. 259 (2024) 129282.
[52] O. Alaysuy, A.Q. Alorabi, M.M. Aljohani, A.A. Alluhaybi, R.M. Snari, N.S. Bedowr, R. Shah, N.M. El-Metwaly, Aluminum MOF-based sensor for simultaneous colorimetric and fluorometric detection of Co+ 2 in electroplating wastewater samples and recovery of Pd+ 2 ions from electronic wastes, J. Water Process Eng. 59 (2024) 104993.
[53] I. Spanopoulos, C. Tsangarakis, E. Klontzas, E. Tylianakis, G. Froudakis, K. Adil, Y. Belmabkhout, M. Eddaoudi, P.N. Trikalitis, Reticular synthesis of HKUST-like tbo-MOFs with enhanced CH4 storage, J. Am. Chem. Soc. 138 (2016) 1568–1574.
[54] C.C. Piras, S. Fernández-Prieto, W.M. De Borggraeve, Ball milling: a green technology for the preparation and functionalisation of nanocellulose derivatives, Nanoscale Adv. 1 (2019) 937–947.
[55] A. Stolle, T. Szuppa, S.E.S. Leonhardt, B. Ondruschka, Ball milling in organic synthesis: solutions and challenges, Chem. Soc. Rev. 40 (2011) 2317–2329.
[56] B. Szczęśniak, S. Borysiuk, J. Choma, M. Jaroniec, Mechanochemical synthesis of highly porous materials, Mater. Horizons 7 (2020) 1457–1473.
[57] X. Wei, X. Wang, B. Gao, W. Zou, L. Dong, Facile Ball-Milling Synthesis of CuO/Biochar Nanocomposites for Efficient Removal of Reactive Red 120, ACS Omega (2020), https://doi.org/10.1021/acsomega.9b03787.
[58] F. Yu, F. Tian, H. Zou, Z. Ye, C. Peng, J. Huang, Y. Zheng, Y. Zhang, Y. Yang, X. Wei, ZnO/biochar nanocomposites via solvent free ball milling for enhanced adsorption and photocatalytic degradation of methylene blue, J. Hazard. Mater. 415 (2021) 125511.
[59] F.L. Chiriac, I. Paun, F. Pirvu, L.F. Pascu, T. Galaon, Occurrence and fate of bisphenol A and its congeners in two wastewater treatment plants and receiving surface waters in Romania, Environ. Toxicol. Chem. 40 (2021) 435–446.
[60] Y. Zheng, Y. Wan, J. Chen, H. Chen, B. Gao, MgO modified biochar produced through ball milling: A dual-functional adsorbent for removal of different contaminants, Chemosphere (2020), https://doi.org/10.1016/j.chemosphere.2019.125344.
[61] A.N. Ebelegi, N. Ayawei, D. Wankasi, Interpretation of adsorption thermodynamics and kinetics, Open J. Phys. Chem. 10 (2020) 166.
[62] M. Behera, N. Tiwari, S. Banerjee, A.R. Sheik, M. Kumar, M. Pal, P. Pal, R. P. Chatterjee, S. Chakrabortty, S.K. Tripathy, Ag/biochar nanocomposites demonstrate remarkable catalytic activity towards reduction of p-nitrophenol via restricted agglomeration and leaching characteristics, Colloids Surfaces A Physicochem. Eng. Asp. 642 (2022) 128616.
[63] U.S.E.P. Agency, Method 1311. Toxicity Characteristic Leaching Procedure, Fed. Regist. 55 (1992) 11798–11877.
[64] D. Zhang, Q. He, X. Hu, K. Zhang, C. Chen, Y. Xue, Enhanced adsorption for the removal of tetracycline hydrochloride (TC) using ball-milled biochar derived from crayfish shell, Colloids Surfaces A Physicochem. Eng. Asp. 615 (2021) 126254.
[65] H. Kwon, M. Leparoux, Hot extruded carbon nanotube reinforced aluminum matrix composite materials, Nanotechnology 23 (2012) 415701.
[66] T.A. Vahed, M.R. Naimi-Jamal, L. Panahi, (Fe) MIL-100-Met@ alginate: a hybrid polymer–MOF for enhancement of metformin's bioavailability and pH-controlled release, New J. Chem. 42 (2018) 11137–11146.
[67] A. Miri, H.O. Shahraki Vahed, M. Sarani, Biosynthesis of silver nanoparticles and their role in photocatalytic degradation of methylene blue dye, Res. Chem. Intermed. 44 (2018) 6907–6915.
[68] Q. Zhang, J. Wang, H. Lyu, Q. Zhao, L. Jiang, L. Liu, Ball-milled biochar for galaxolide removal: Sorption performance and governing mechanisms, Sci. Total Environ. (2019), https://doi.org/10.1016/j.scitotenv.2019.01.005.
[69] S. Yumitori, Correlation of C1s chemical state intensities with the O1s intensity in the XPS analysis of anodically oxidized glass-like carbon samples, J. Mater. Sci. 35 (2000) 139–146.
[70] M. Kumar, X. Xiong, Z. Wan, Y. Sun, D.C.W. Tsang, J. Gupta, B. Gao, X. Cao, J. Tang, Y.S. Ok, Ball milling as a mechanochemical technology for fabrication of novel biochar nanomaterials, Bioresour. Technol. (2020), https://doi.org/10.1016/j.biortech.2020.123613.
[71] G. Crini, P.-M. Badot, Application of chitosan, a natural aminopolysaccharide, for dye removal from aqueous solutions by adsorption processes using batch studies: A review of recent literature, Prog. Polym. Sci. 33 (2008) 399–447.
[72] T.G. Kebede, S. Dube, V. Mhuka, M.M. Nindi, Bioremediation of Cd (II), Pb (II) and Cu (II) from industrial effluents by Moringa stenopetala seed husk, J. Environ. Sci. Heal. Part A 54 (2019) 337–351.
[73] S.O. Amusat, T.G. Kebede, E.N. Nxumalo, S. Dube, M.M. Nindi, Green Synthesis of Surface Modified Biochar for Simultaneous Removal of Steroidal Hormones and Heavy Metals from Wastewater: Optimisation by Central Composite Design, Water 15 (2023) 3703.
[74] M. Zhang, B. Gao, Y. Yao, Y. Xue, M. Inyang, Synthesis of porous MgO-biochar nanocomposites for removal of phosphate and nitrate from aqueous solutions, Chem. Eng. J. 210 (2012) 26–32.
[75] Y. Zhou, B. Gao, A.R. Zimmerman, H. Chen, M. Zhang, X. Cao, Biochar-supported zerovalent iron for removal of various contaminants from aqueous solutions, Bioresour. Technol. 152 (2014) 538–542, https://doi.org/10.1016/j.biortech.2013.11.021.
[76] E. Agrafioti, D. Kalderis, E. Diamadopoulos, Ca and Fe modified biochars as adsorbents of arsenic and chromium in aqueous solutions, J. Environ. Manage. (2014), https://doi.org/10.1016/j.jenvman.2014.07.029.
[77] T. Liu, B. Gao, J. Fang, B. Wang, X. Cao, Biochar-supported carbon nanotube and graphene oxide nanocomposites for Pb(II) and Cd(II) removal, RSC Adv. (2016), https://doi.org/10.1039/c6ra01895e.
[78] M.C. Wang, G.D. Sheng, Y.P. Qiu, A novel manganese-oxide/biochar composite for efficient removal of lead (II) from aqueous solutions, Int. J. Environ. Sci. Technol. 12 (2015) 1719–1726.
[79] C.L. Johansson, N.A. Paul, R. de Nys, D.A. Roberts, Simultaneous biosorption of selenium, arsenic and molybdenum with modified algal-based biochars, J. Environ. Manage. 165 (2016) 117–123.
[80] H. Li, X. Dong, E.B. da Silva, L.M. de Oliveira, Y. Chen, L.Q. Ma, Mechanisms of metal sorption by biochars: Biochar characteristics and modifications, Chemosphere 178 (2017) 466–478, https://doi.org/10.1016/j.chemosphere.2017.03.072.
[81] M.B. Ahmed, J.L. Zhou, H.H. Ngo, W. Guo, M.A.H. Johir, K. Sornalingam, D. Belhaj, M. Kallel, Nano-Fe0 immobilized onto functionalized biochar gaining excellent stability during sorption and reduction of chloramphenicol via transforming to reusable magnetic composite, Chem. Eng. J. (2017), https://doi.org/10.1016/j.cej.2017.04.063.
[82] D. Chen, C. Chen, W. Shen, H. Quan, S. Chen, S. Xie, X. Luo, L. Guo, MOF-derived magnetic porous carbon-based sorbent: synthesis, characterization, and adsorption behavior of organic micropollutants, Adv. Powder Technol. 28 (2017) 1769–1779.
[83] W. Sun, C. Zhang, N. Xu, J. Ni, Effect of inorganic nanoparticles on 17β-estradiol and 17α-ethynylestradiol adsorption by multi-walled carbon nanotubes, Environ. Pollut. 205 (2015) 111–120.
[84] M. Inyang, B. Gao, A. Zimmerman, M. Zhang, H. Chen, Synthesis, characterization, and dye sorption ability of carbon nanotube-biochar nanocomposites, Chem. Eng. J. (2014), https://doi.org/10.1016/j.cej.2013.09.074.
[85] V.K. Gupta, S. Agarwal, T.A. Saleh, Synthesis and characterization of alumina-coated carbon nanotubes and their application for lead removal, J. Hazard. Mater. 185 (2011) 17–23.
[86] G. Zhao, J. Li, X. Ren, C. Chen, X. Wang, Few-layered graphene oxide nanosheets as superior sorbents for heavy metal ion pollution management, Environ. Sci. Technol. 45 (2011) 10454–10462.
[87] G.P. Rao, C. Lu, F. Su, Sorption of divalent metal ions from aqueous solution by carbon nanotubes: a review, Sep. Purif. Technol. 58 (2007) 224–231.
[88] V.-K.-M. Au, Recent advances in the use of metal-organic frameworks for dye adsorption, Front. Chem. 8 (2020) 708.
[89] J. Abdi, M. Vossoughi, N.M. Mahmoodi, I. Alemzadeh, Synthesis of metal-organic framework hybrid nanocomposites based on GO and CNT with high adsorption capacity for dye removal, Chem. Eng. J. 326 (2017) 1145–1158.